Numerical Sturdy of Electrode Geometry Effects on Flowfield in Two-dimensional MPD Thrusters

IEPC-2007-87

Presented at the 30th International Electric Propulsion Conference, Florence, Italy
September 17-20, 2007

K. Kubota*
Tokyo Institute of Technology, Yokohama, Kanagawa, 226-8502, Japan
I. Funaki†
Japan Aerospace Exploration Agency, Sagamihara, Kanagawa, 229-8510, Japan

Y. Okuno‡
Tokyo Institute of Technology, Yokohama, Kanagawa, 226-8502, Japan

Numerical study of the geometry effect on the flowfield in Two-dimensional MPD Thrusters (TMPDT) is conducted under the constant mass flow rate 1.25 g/s for argon propellant. Employed anodes are converging-diverging anode, flared anode, and straight anode. As for the cathode, short cathode and embedded cathode are examined. The results of the self-field TMPDT show that the embedded cathode can enhance the thrust and thrust efficiency. In addition, an external magnetic field which assists the induced magnetic field is applied to the TMPDT. In this study, with cylindrical alnico magnet, the thrust and thrust efficiency are improved. The highest thrust efficiency about 0.16 is accomplished at 16 kA for the geometry with a converging-diverging anode and a embedded cathode.

Nomenclature

$\boldsymbol{B}_i, \boldsymbol{B}_a$	= Induced, and Applied Magnetic flux density
$\boldsymbol{E}$	= Electric field vector
e	= Elementary charge
F	= Thrust
$\boldsymbol{I}$	= Unit tensor
J	= Discharge current
$\boldsymbol{j}$	= Current density
k	= Boltzmann constant
$\dot{m}$	= Mass flow rate
n_s	= Number density of particle s
p	= Pressure
$\boldsymbol{q}$	= Heat flux vector
T	= Temperature
U_s	= Internal energy of particles s
U_i	= Total ionization energy
$\boldsymbol{u}$	= Velocity vector

*Graduate Student, Department of Energy Sciences, E-mail: d06kubota@es.titech.ac.jp
†Associate Professor, Institute of Space and Astronautical Science E-mail: funaki@isas.jaxa.jp
‡Professor, Department of Energy Sciences, E-mail: yokuno@es.titech.ac.jp

V = Voltage
V_i = Ionization energy from i-1 to i-fold ionization level
V_s = Sheath voltage
W = Width of the thruster
x = x-coordinate
x_c, y_c = Location of the coil center
y = y-coordinate
μ_0 = Permeability
ρ = Mass density
σ = Electrical conductivity
$\boldsymbol{\tau}$ = Viscous stress tensor
Φ = Dissipation function

Subscript
e = Electrons
h = Heavy particles

I. Introduction

THE Self-field MagnetoPlasmaDynamic Thruster (SMPDT) is a promising candidate as a propulsion device for an interplanetary exploration. In a SMPDT, the Lorentz force obtained from the discharge current and the induced magnetic field accelerates the plasma generated by the arc discharge. Since the general SMPDTs consist of coaxial electrodes, it is hard to observe the flow fields in the thrusters.

In the late 1980s, Toki et al. developed a Self-field Two-dimensional MPD Thruster (STMPDT) as shown in Fig.1 in order to measure the density, temperature, and current distribution via optical techniques.[1] In the 1990s, Funaki et al. conducted the investigations on the geometry optimizations by means of the experiments and numerical simulations with the simple model, where the fully ionization was assumed, but viscosity, thermal conduction, and Hall effect were ignored.[2,3] According to the results obtained by Funaki, the short cathode is superior to the long cathode in the medium-I_{sp} range between 1000-3000 s.

Actually the STMPDT was originally designed just for the plasma observation, although it is very difficult to reflect the features of coaxial devices. However the abundant experimantal data will be helpful to validate our numerical results, and to check and/or make a physical model inside the thruster. In addition, the correlation between the flowfield and the thruster performance will contribute to offer a design policy for MPD arcjets with its preferred acceleration mechanisms.

In this paper, we examine a variety of configurations of STMPDT in the medium-I_{sp} range by the numerical simulation with the state-of-the-art detailed numerical modeling. Especially, not only the anode geometries effect but also the cathode geometries effect on the thrust performance are discussed.

In addition to the self-field MPD thrusters, Applied-field MPD Thrusters (AMPDT) have been studied for many years. In general, AMPDTs have an external circular coil surrounding the axisymmetric anode. The interaction between the external magnetic field and the discharge current induces the plasma rotation and the azimuthal Hall current, which lead to the swirl and the Hall acceleration. On the other hand, when we consider an Applied-field Two-dimensional MPDT (ATMPDT), the same idea as that of the axisymmetric MPDT can not be employed. However, if the external magnetic field is applied so that the applied field assists the induced field as shown in Fig.2, the Lorentz force can be controlled explicitly. If the thrust efficiency of STMPDTs is improved by applying the magnetic field, there is a possibility that the performance of two-dimensional MPDTs is equal to or excess that of the coaxial MPD thrusters. Thus, in this paper, the flowfield simulation on the ATMPDT as well as the STMPDT is studied, and comparisons of the thrust, voltage, and thrust efficiency with those of STMPDTs are conducted.

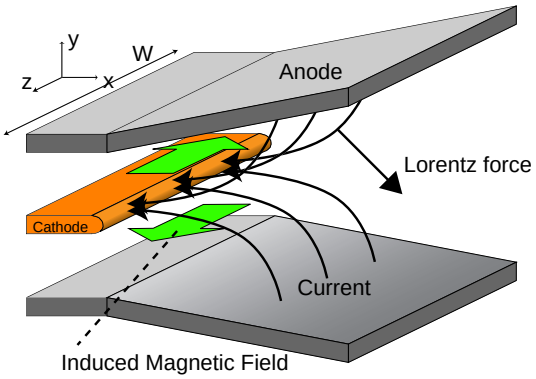

Figure 1. Principle of a Self-field Two-dimensional MPD Thruster.

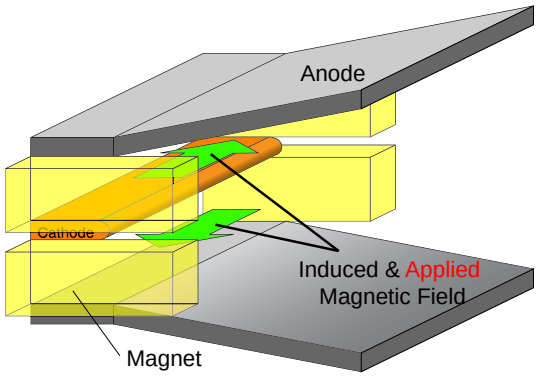

Figure 2. Concept of an Applied-field Two-dimensional MPD Thruster.

II. Numerical Modeling

II.A. Thruster Geometries

The thrusters examined in this paper have Converging-Diverging Anode (CDA), Flared Anode (FA), Straight Anode (SA), which were investigated by Funaki (Figs.3(a)-3(c)). In addition, two geometries which have the embedded cathode (EC) as shown in Fig.3(d)(ECCDA), and 3(e)(ECFA) are analyzed. The inner height of the anode at the inlet is 14 mm except for the ECFA. This cathode design is based on the experimental evidence that the thrust efficiency is improved by shortening the cathode.[2] With this cathode, we expect to obtain the higher pumping force. Let us refer to the abbreviated words in parentheses shown in Fig.3 in this paper. The width of the thruster W is set to 80 mm.

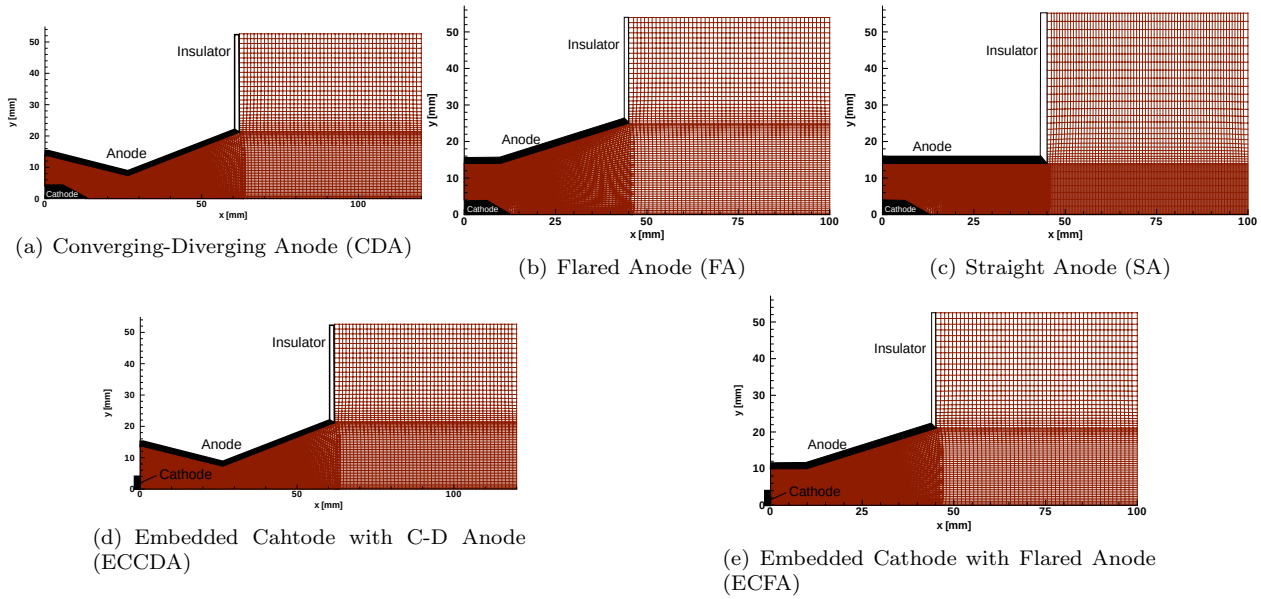

(a) Converging-Diverging Anode (CDA)

(b) Flared Anode (FA)

(c) Straight Anode (SA)

(d) Embedded Cahtode with C-D Anode (ECCDA)

(e) Embedded Cathode with Flared Anode (ECFA)

Figure 3. Thruster Geometries and Computational Regions.

II.B. Basic Equations

In this study, argon is used as a propellant, and we include non-equilibrium multivalent ionization up to Ar^{2+} in our numerical code. The Navier-Stokes equation with the MHD effect, and the induction equation, which determines the induced magnetic field have to be solved. In the formulation, we assumed the flow is completely uniform in the direction of the z axis. When the applied magnetic field $\boldsymbol{B}_a = (0, 0, B_a)$ exists, $\boldsymbol{B}_a$ has to be distinguished from the induced magnetic field $\boldsymbol{B}_i$. The basic equations including $\boldsymbol{B}_t = \boldsymbol{B}_i + \boldsymbol{B}_a$ are as follows.

Total mass density

$$\frac{\partial \rho}{\partial t} + \nabla \cdot \rho \boldsymbol{u} = 0 \tag{1}$$

Mass density of s-fold ion ($s = 1, 2$)

$$\frac{\partial \rho_s}{\partial t} + \nabla \cdot \rho_s \boldsymbol{u} = \dot{\rho}_s \tag{2}$$

Momentum

$$\frac{\partial \rho \boldsymbol{u}}{\partial t} + \nabla \cdot \left(\rho \boldsymbol{u}\boldsymbol{u} + \left(p + \frac{\boldsymbol{B}_i^2}{2\mu_0} \right) \boldsymbol{I} - \frac{\boldsymbol{B}_i \boldsymbol{B}_i}{\mu_0} \right) = \boldsymbol{j} \times \boldsymbol{B}_a + \nabla \cdot \boldsymbol{\tau} \tag{3}$$

Energy

$$\frac{\partial U_h}{\partial t} + \nabla \cdot (U_h \boldsymbol{u}) = -p_h \nabla \cdot \boldsymbol{u} + \Phi - \nabla \cdot \boldsymbol{q}_h + \Delta E \tag{4}$$

$$\frac{\partial (U_e + U_i)}{\partial t} + \nabla \cdot ((U_e + U_i)\boldsymbol{u}) = -p_e \nabla \cdot \boldsymbol{u} + \frac{\boldsymbol{j}^2}{\sigma} - \nabla \cdot \boldsymbol{q}_e - \Delta E \tag{5}$$

Induction Equation

$$\frac{\partial \boldsymbol{B}_t}{\partial t} - \nabla \times (\boldsymbol{u} \times \boldsymbol{B}_t) = -\nabla \times \left(\frac{1}{\sigma \mu_0} \nabla \times \boldsymbol{B}_i \right) + \nabla \times \left(\frac{1}{e n_e \mu_0} (\nabla \times \boldsymbol{B}_i) \times \boldsymbol{B}_t \right) \tag{6}$$

The right hand side of the Eq. (2) denotes the reaction source term which describes the ionization rates and the recombination rates.[4] Lotz formula is utilized as the forward reaction rates,[5] and the recombination rates are given from the forward rates and equilibrium constants. The source term of the Eq. (3) is the viscous term, and the second term in the source term of the Eq. (4) is the dissipation function. The internal energy of the heavy particles and electrons are defined as $U_s = \frac{3}{2} n_s k T_s (s = h, e)$. The total ionization energy U_i is given by $\sum_{s=1}^{6} (\sum_{1}^{s} V_i) n_s$. The $\boldsymbol{q}_s$ and ΔE are the thermal flux vector and the energy exchange rate between the heavy particles and electrons respectively.[6] The cross sections and viscous, thermal conductivity coefficients are computed with the equations found in Ref. 20. The other equations necessary for the complete formulation are Ohm's law, Maxwell equation, and equation of state.

$$\boldsymbol{j} = \frac{1}{\mu_0} \nabla \times \boldsymbol{B}_i \tag{7}$$

$$\boldsymbol{E} = \frac{\boldsymbol{j}}{\sigma} - \boldsymbol{u} \times \boldsymbol{B}_t + \frac{1}{e n_e} \boldsymbol{j} \times \boldsymbol{B}_t \tag{8}$$

$$p = p_h + p_e = n_h k T_h + n_e k T_e \tag{9}$$

The governing equations (1)-(6) in the preceding sections are solved numerically by a time marching method. All equations are integrated with high order Lax-Friedrich TVD scheme.[7,8]

II.C. Boundary Conditions

In this study, the propellant injected from the inlet is argon, and the prescribed mass flow rate is 1.25 g/s. Since the consideration of the plasma ignition at the inlet is difficult to incorporate into the numerical simulation, we ignore the processes and assume a relatively high temperature and highly ionized plasma inflows into the thruster. Thus the enthalpy flux, which corresponds to the sum of the flux of kinetic, internal, ionization, and pressure energy, is set to 8 kW at the inlet in this calculation. Moreover we set the ionization fraction at the inlet to 0.06.[9] As for the pressure at the inlet, the value next to the inlet is extrapolated. Then the electron temperature is assumed to be the same as the heavy particle temperature at the inlet.

In order to take account of the heat transfer from the plasma to the wall, we set the heavy particle temperature to 1300 K on the anode surface and to 2000 K on the cathode surface. For the boundary condition of the electron temperature along the wall, the adiabatic condition is adopted.

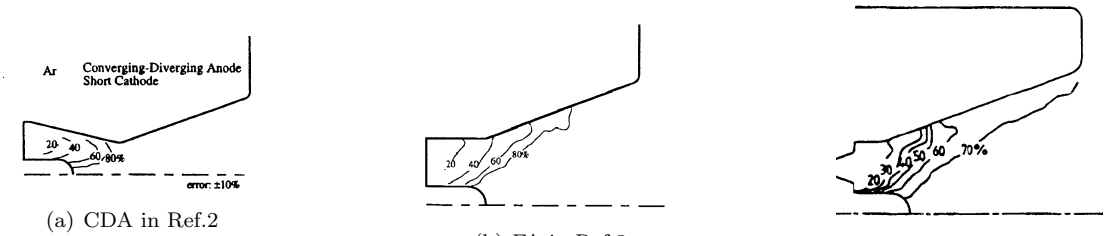

(a) CDA in Ref.2

(b) FA in Ref.3

(c) FA in Ref.1

Figure 4. Experimental Results of the Current Paths ($\dot{m}$=1.25 g/s, J = 12 kA, Ar).

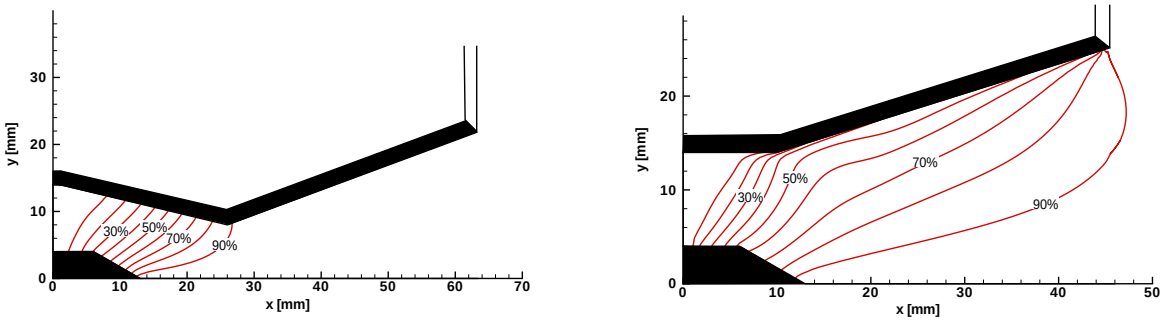

(a) CDA

(b) FA

Figure 5. Current Path for the Geometry of CDA, and FA ($\dot{m}$ = 1.25 g/s, J = 12 kA, Ar).

The total discharge current J, which determines the distribution of the magnetic flux density at the inlet, is varied over the range 8 - 16 kA. The magnetic flux density at the inlet is obtained from the Ampere's law.

$$B_{in} = -\frac{\mu_0 J}{2W} \tag{10}$$

As for the magnetic flux density along the wall, it is determined from the condition that the tangential component of the electric field is zero. On the insulator, the magnetic flux density is set to zero.

III. Results of Self-field Two-dimensional MPD Thrusters

In this section, the numerical results of the STMPDTs are discussed in comparison with the experimental results.

III.A. Comparison with the Experimental data

Comparisons with the experimental data obtained by Funaki et al. and Toki et al. have been conducted in order to validate the numerical results. In this paper, current path and electron density distributions for the geometries of CDA and FA are compared. After the comparisons, the flowfield of the geometry with the EC are discussed, and thrust efficiency for each geometry is evaluated.

III.A.1. Current Path

Figure 4 shows the experimental results of the current path for the C-D anode and Flared anode measured by Funaki,[2,3] and Toki[1] by using a magnetic sensitive films with microencapsulated iron needles. Moreover, the numerical results of the current paths for geometries of CDA, and FA are described in Fig.5.

As for the CDA, the numerical result is similar to the experimental one in that 80% of the discharge current are confined within the converging part, although the current path of the experimental results near the anode is distorted compared with the numerical results for some reason. On the other hand, the current path for the FA expands toward the downstream region. Although there are some differences between the results of Fig.4(b), and 4(c), it is reasonable to suppose that about 20-30% of the discharge current concentrates at the anode edge, and this tendency also appears in the numerical results. This skewed current profile is considered to be caused by the Hall effect.[11]

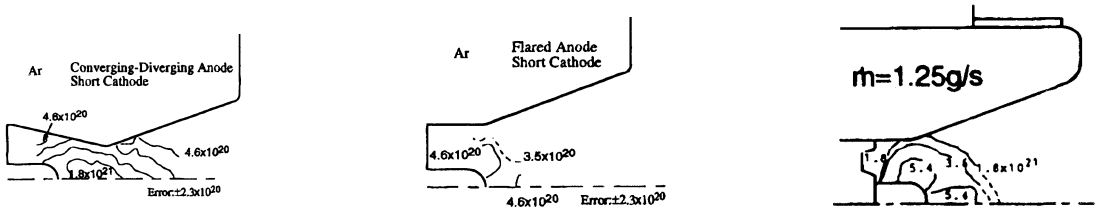

(a) CDA in Ref.2

(b) FA in Ref.2

(c) FA in Ref.10

Figure 6. Experimental Results of the Plasma Density, m^{-3} ($\dot{m}$=1.25 g/s, J = 12 kA, Ar).

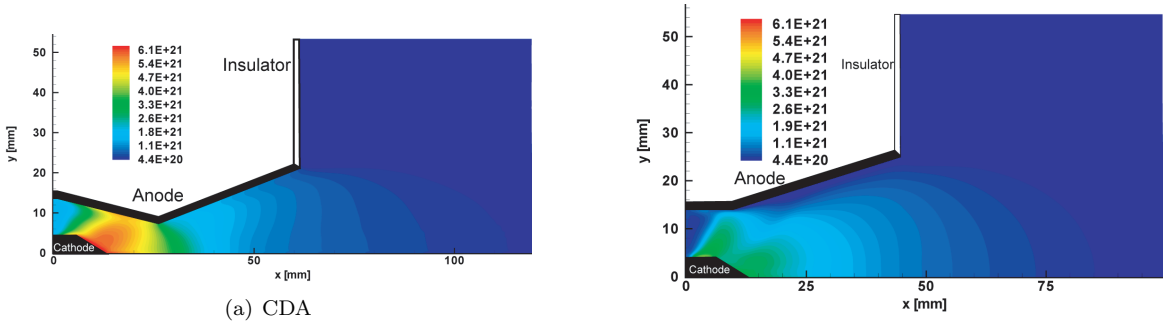

(a) CDA

(b) FA

Figure 7. Electron Number Densiy for the Geometry of CDA, and FA, m^{-3} ($\dot{m}$ = 1.25 g/s, J = 12 kA, Ar).

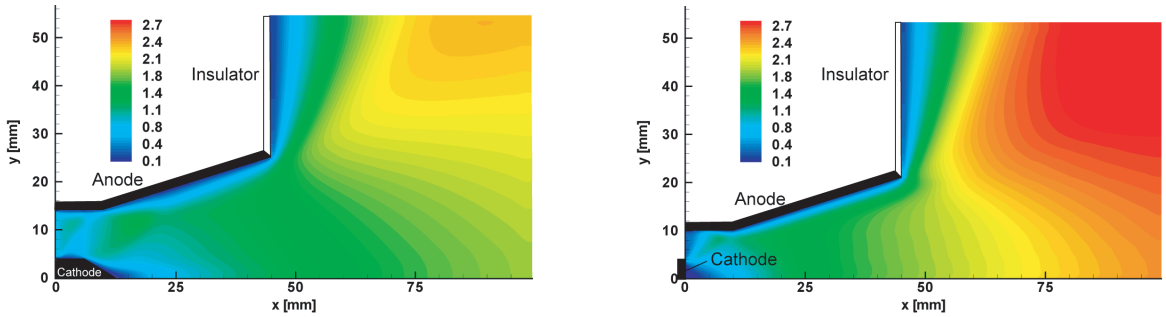

(a) FA

(b) ECFA

Figure 8. Mach Number Distribution for the Geometry of FA, and ECFA ($\dot{m}$ = 1.25 g/s, J = 12 kA, Ar).

III.A.2. Electron Number Density

Figure 6 shows the experimental results of the electron number density n_e. While the n_e measured by Funaki shown in Fig.6(a), and 6(b) is in the order of 10^{20} m^{-3} in the almost whole region, the n_e obtained by Nakayama shown in Fig.6(c) is in the order of 10^{21} m^{-3}. This difference may result from the leak of the propellant from the thruster side, and some sort of the operation condition.

As far as the distribution is concerned, the numerical results for the CDA and FA are similar to those of Fig.6(a) and 6(b) respectively, although there is quantitative disagreement. Our numerical result of FA relatively agrees with the results of Fig.6(c) quantitatively as well as qualitatively. As this calculation assumes the constant inlet ionization fraction 0.06, quantitative disagreement will be reduced via more reasonable selection of this value.

On the whole, our numerical results seem to provide reasonable solutions for the flowfield in STMPDT. In the following part, let us proceed to analyze the flows in the other geometries.

III.B. Flowfield with Embedded Cathode Type Geometry

Funaki suggested that a compression wave produced by the high-density and high-temperature region around the cathode tip may degrade aerodynamic acceleration.[2] In order to examine this suggestion, the Mach number distribution for FA is described in Fig.8(a). Although the Mach number increases along the stream

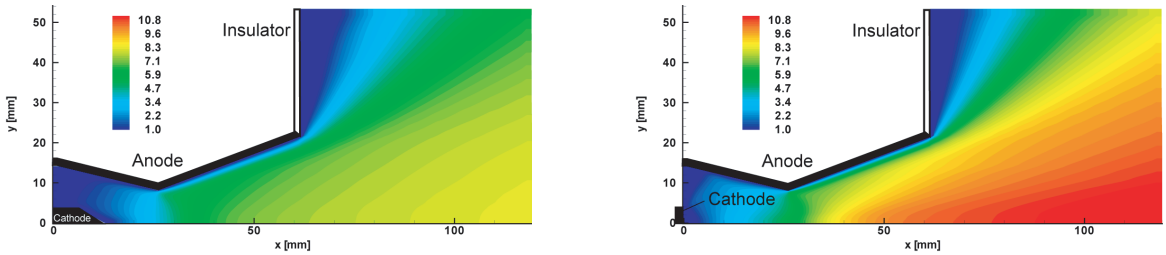

(a) CDA (b) ECCDA

Figure 9. Velocity in x direction for CDA, and ECCDA, km/s. ($\dot{m}$ = 1.25 g/s, J = 12 kA, Ar).

on the whole, it is locally decreased around $x = 6$, and 20 mm. First decrease is due to the compression wave produced at the cathode root, which results from the intensive current concentration at that point. Second decrease is attributed to the compression wave from the cathode tip. Consequently, the Mach number reaches only about 1.3 at the thruster exit. These compression waves seem to spoil the acceleration by the flared nozzle.

On the other hand, the EC type thruster is expected to avoid this deceleration, because the cathode is completely embedded. To compare the flowfield with that of FA, the Mach number distribution for the ECFA is shown in Fig.8(b). It can be seen that the deceleration does not occur in the flared region, where the flow is supersonic, and the Mach number at the thruster exit reaches about 1.8. Therefore the EC configuration is considered to be effective for the acceleration.

As for the CDA, there is no deceleration in the supersonic region as shown in Fig.9(a), because the high pressure region is confined within the subsonic region $x < 26$ mm(throat), which can also be seen from Fig.7(a), thus a strong compression wave does not appear. However the velocity in x direction is increased drastically by employing the EC (Fig.9(b)) due to an increase in the pumping force. The pressure at the cathode tip is about 7 $\times 10^3$ Pa in the case of ECCDA, while it is about 5 $\times 10^3$ Pa for the CDA.

III.C. Performance Evaluation of STMPDT

The thrusts F are plotted in Figs.10. The F is computed by the momentum flux at the thruster exit.

$$F = \int_{exit} (\rho u^2 + p) dS \tag{11}$$

As for the thrusters with the short cathode (CDA, FA, SA), FA produces the highest thrust under the same current, which agrees with the experimental results.[12] We can see that the thrusters with the EC (ECCDA, ECFA) have the higher thrusts (2 - 3 N) than the thrusters with the short cathode owing to the absence of the drastic deceleration caused by the compression wave.

Figure 11 shows the voltages evaluated by the line integral of the electric field from the anode to cathode, where the sheath voltage is not included. In the case of the thrusters with the short cathode, CDA keeps the discharge voltage low for the whole operation range due to its short electrode interval, while the voltage of FA increases rapidly. As for the thrusters with the EC geometry, the voltage is higher than the others, and both ECFA and ECCDA show similar tendency.

The thrust efficiency η of each geometry is evaluated based on the thrust and voltage, and is plotted in Fig.12. The η is evaluated with the following equation.

$$\eta = \frac{(F - F_{in})^2}{2\dot{m}J(V + V_s)} \tag{12}$$

F_{in} denotes the momentum flux at the inlet $\dot{m}\bar{u}_{in}$, where $\bar{u}_{in}$ is the average velocity in x direction. Since the actual thruster's injection port is small, the pressure at the inlet is supposed to press the backplate part. Thus the pressure at the inlet is not included for the evaluation of the F_{in}. In the Fig.12, the discharge currents for the geometries CDA, and ECCDA, are 8, 10, 12, 16 kA, and for the others are 8, 10, 12 kA. The sheath voltage V_s is assumed as 20 V.

Among the thrusters with the short cathode, CDA accomplishes the highest thrust efficiency about 0.11 at 510 kW. The superiority of CDA compared with FA, and SA in this operation range was also indicated by

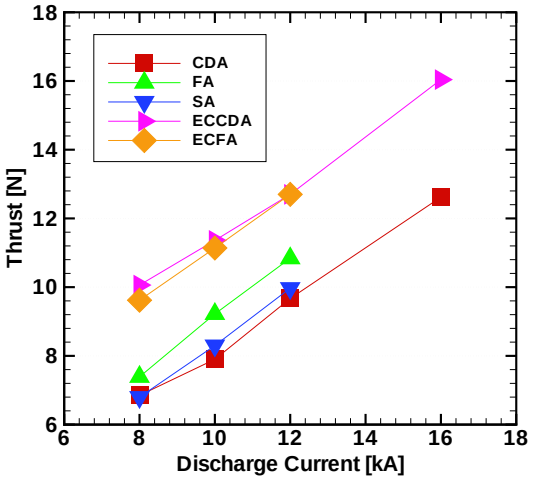

Figure 10. Thrust vs Discharge Current ($\dot{m}$ = 1.25 g/s, Ar).

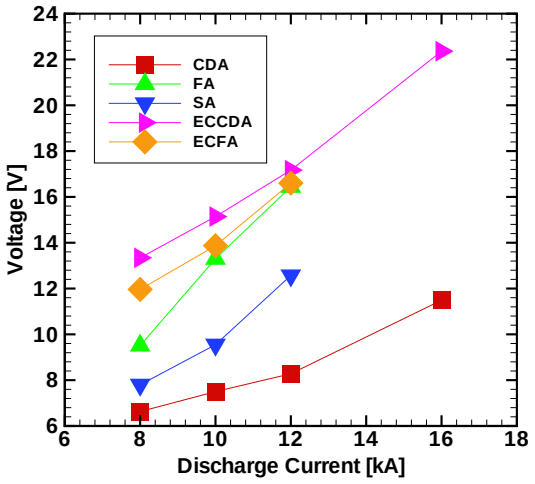

Figure 11. Voltage vs Discharge Current. The sheath voltage is not included. ($\dot{m}$ = 1.25 g/s, Ar).

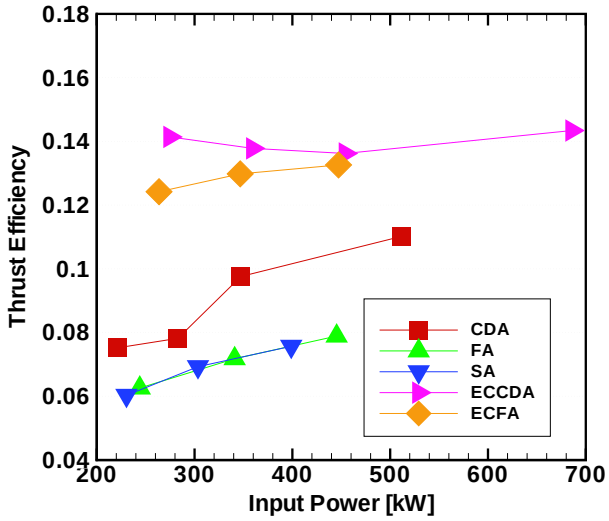

Figure 12. Thrust Efficiency vs Input Power. The discharge currents for the geometries CDA, and ECCDA, are 8, 10, 12, 16 kA, and for the others are 8, 10, 12 kA. The sheath voltage V_s is assumed as 20 V. ($\dot{m}$ = 1.25 g/s, Ar).

the experiment.[2] On the other hand, the results shows that η is drastically enhanced by using the EC. The η of both ECCDA and ECFA reaches about 0.12 - 0.14 for the whole operation range, which is attributed to the increased thrust.

IV. Results of Applied-field Two-dimensional MPD Thrusters

In this section, the flowfields in the ATMPDTs are discussed. At first, how to determine the applied field is explained, and after that, the change in the performances are shown.

IV.A. Applied Magnetic field Distribution

If magnets to produce the applied field are located at the both side of the thruster as shown in Fig.2, the magnetic field has a three-dimensional structure in the thruster. Since the present numerical code can not analyze the three-dimensional flowfield, we have to consider an averaged magnetic field in z direction. However, if we set the width of the two-dimensional MPDT to 80 mm as before, the magnetic field strength produced by a finite size magnet will decrease significantly around the middle part of the thruster. Therefore let us assume an ideal situation that some magnets are located in z direction separately with a reasonable

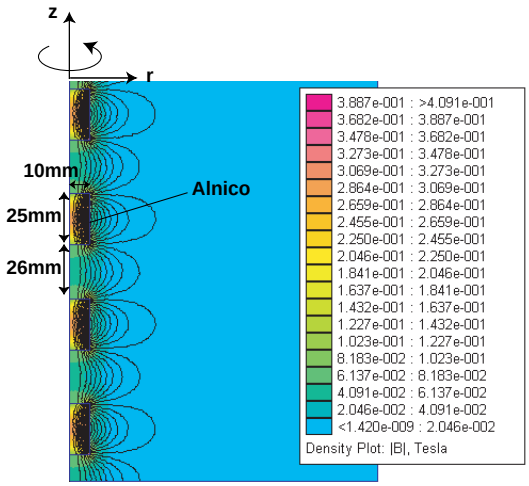

Figure 13. Applied Magnetic Field Analysis.

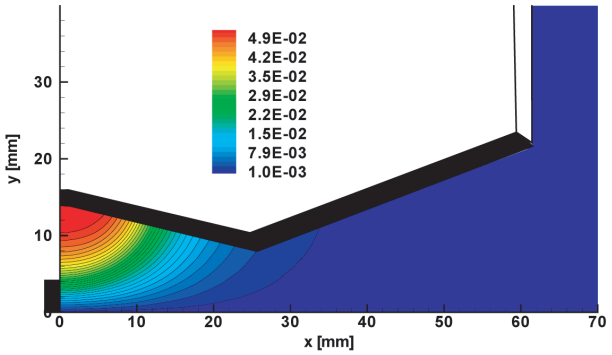

Figure 14. Applied Magnetic Field Distribution, T. The center of the magnet is located at (x_c, y_c)=(0,15mm), and the oppositely magnetized one at (0,-15mm).

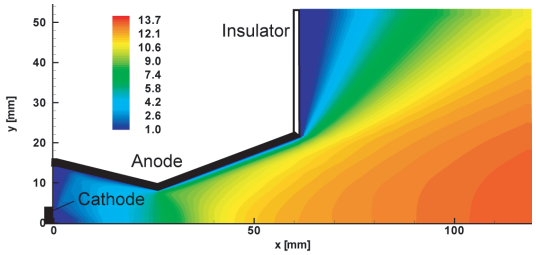

(a) Without Applied Magnetic Field

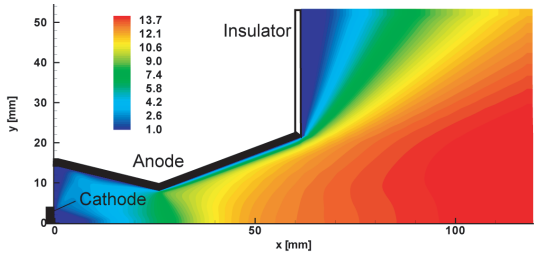

(b) With Appleid Magnetic Field

Figure 15. Velocity in x direction, km/s. a) Without Applied Magnetic Field, b) With Applied Magnetic Field, x_c = 0mm. ($\dot{m}$ = 1.25 g/s, J = 16 kA, Ar).

interval, and the two-dimensional MPDT is divided and set between the magnets.

In this study, cylindrical alnico magnets are assumed as the magnets, and the applied magnetic field distribution is determined from the magnetic field analysis shown in Fig.13. In this analysis, cylindrical alnico magnets, which are 10 mm in radius and 25 mm in length, are arranged lengthwise. The interval between the magnets is 26 mm. With this condition, we can divide the MPDT with 80 mm in width into the four thrusters with 20 mm in width, and can set each one between the magnets with ease. The rest of the gaps can be filled with some adiabatic material not to deteriorate the magnet, and to prevent the leak of the propellants.

From the calculated results of the magnetic field, we calculate the average magnetic field in z direction and obtain the averaged radial distribution of the magnetic field as shown in Fig.14. Since the magnets which have opposite magnetization are located at the downside, the applied magnetic field is zero on the x axis. The magnetic flux density at the center of the magnet is about 0.05 T under the present condition, which is the same order with the induced magnetic field.

In this paper, the flowfields with the applied magnetic field for the geometries with the EC are computed.

IV.B. Flowfield of the ATMPDTs

In this section, we discuss the change in the flowfield caused by the presence of the applied magnetic field. Figure 15 shows the velocity in x direction for the geometry ECCDA, where the discharge current is 16 kA. With the applied magnetic field, the velocity at the thruster exit amounts to 13.2 km/s, while it is 12.2 km/s in the case without the applied magnetic field. This result suggests that the applied magnetic field can enhance the thrust for constant current. However, the magnetic field perpendicular to the stream results in an increase in the discharge voltage, thus if the thrust efficiency is improved or not has to be examined. The thrust efficiency is discussed later.

In order to examine the magnet location effect, current paths for two cases of the magnet location are described in Fig.16, where the locations are $x_c = 0, 30$ mm. We can see that the current path with $x_c = 30$

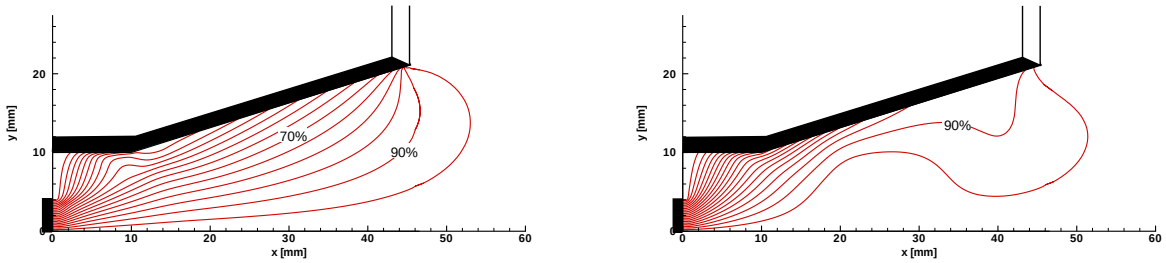

(a) $x_c = 0$ mm (b) $x_c = 30$ mm

Figure 16. Effect of Coil Location on Current Path. ($\dot{m}$ = 1.25 g/s, J = 12 kA, Ar).

mm is distorted around the coil compared with that with $x_c = 30$ mm, which is due to the back electro motive force. Since the current flowing toward the anode, which occurs around $x = 30$mm, produces the Lorentz force toward the upstream region, the current distortion in Fig.16(b) is considered to prevent smooth acceleration. Actually, the thrust efficiency of the case with $x_c = 30$ mm is reduced, therefore the coil should be located around the inlet.

IV.C. Performance of the ATMPDTs

The thrust and the voltage for the geometries ECCDA, and ECFA with and without the applied field are plotted in Figs.17, and 18. As the current is increased, the increment of the thrust is enlarged for the both geometries. The highest thrust in this paper is 18 N which is obtained with the ECCDA at 16 kA. Similarly, the increment of the voltage is also increased with rising discharge current. It can be seen that the applied magnetic field leads to the increase in the discharge voltage about 5 V at most.

As for the thrust efficiency evaluated with Eq.12, the applied magnetic field contributes to increase the η over almost whole power range as shown in Fig.19. The figure suggests that the increase in the η is notable as the input power is high. The highest thrust efficiency about 0.16 is accomplished with the ECCDA at 16 kA.

V. Conclusion

Geometry effect on the flowfields of the two-dimensional MPD thrusters are numerically examined under the constant mass flow rate 1.25 g/s of argon propellant. The examined geometries include a converging-diverging anode (CDA), flared anode (FA), and straight anode (SA) with a short cathode, which are employed in the past experiment. In addition, geometries of the CDA and FA with a embedded cathode (EC) are also analyzed (ECCDA,ECFA). The validation of the numerical code is conducted by the comparisons with the experimental results for such data as the current paths and electron number density. It is found that the embedded cathode can drastically improve the thrust about 2 - 3 N and thrust efficiency. In the ECFA flowfield, a compression wave from the cathode tip does not disturb the supersonic flowfield. Although there is no deceleration in the supersonic region in the CDA, the embedded cathode is attributed to the performance improvement due to the increment in the pumping force.

Moreover applied-field two-dimensional MPD thrusters are also discussed. The results suggests that the location of the magnets should be around the upstream region in order to avoid the high back electro motive force in the downstream region. It is also shown that the applied magnetic field leads to an increase in the thrust and thrust efficiency. The highest thrust efficiency about 0.16 is accomplished at 16 kA for the geometry with a converging-diverging anode and a embedded cathode.

Acknowledgments

This work is supported by the Center for Planning and information Systems in Institute of Space and Astronautical Science.

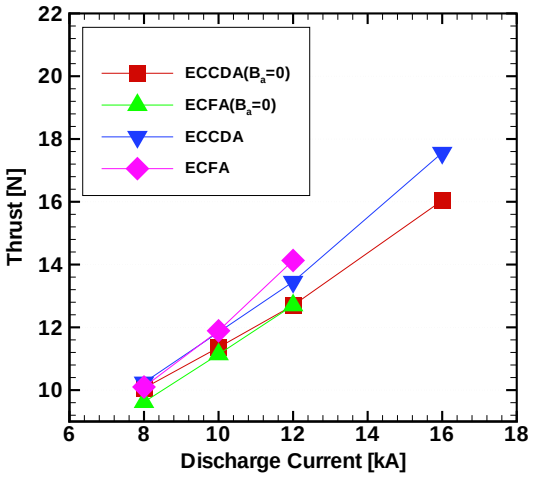

Figure 17. Thrust vs Discharge Current of the ATMPDTs. ($\dot{m}$ = 1.25 g/s, Ar).

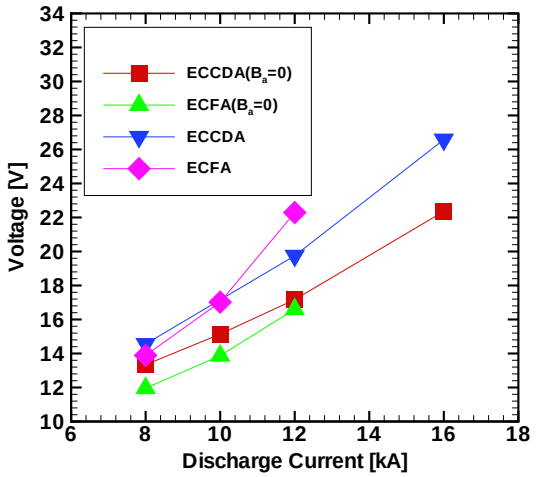

Figure 18. Voltage vs Discharge Current of the ATMPDTs. The sheath voltage is not included. ($\dot{m}$ = 1.25 g/s, Ar).

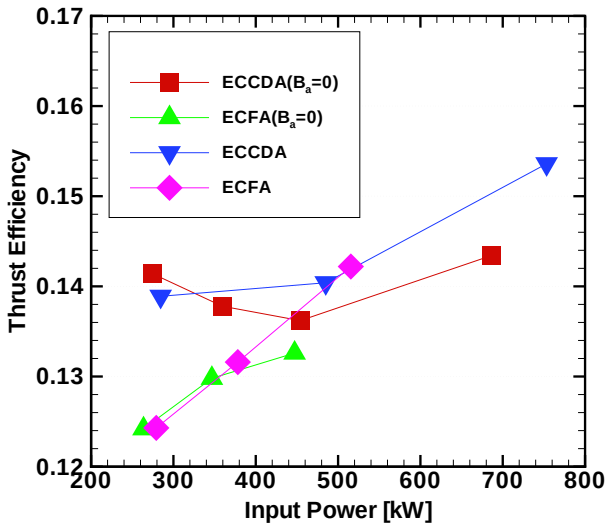

Figure 19. Thrust Efficiency vs Input Power of the ATMPDTs. The sheath voltage V_s is assumed as 20 V. ($\dot{m}$ = 1.25 g/s, Ar).

References

[1]Toki, K., Sumida, M, and Kuriki, K. "Multichannel Two-Dimensional Magnetoplasmadynamic Ardjet," *Journal of Propulsion and Power*, Vol. 8, No. 1, 1992, pp. 93-97.

[2]Funaki, I., Toki, K., and Kuriki, K., "Electrode Configuration Effect on the Performance of a Two-Dimensional Magnetoplasmadynamic Arcjet," *Journal of Propulsion and Power*, Vol. 14, No. 6, 1998, pp. 1043-1048.

[3]Funaki, I., Toki, K., and Kuriki, K., "Numerical Analysis of a Two-Dimensional Magnetoplasmadynamic Arcjet," *Journal of Propulsion and Power*, Vol. 13, No. 6, 1997, pp. 789-795.

[4]Heiermann, J., and Auweter-Kurtz, M., "Numerical and Experimental Investigation of the Current Distribution in Self-Field Magnetoplasmadynamic Thrusters," *Journal of Propulsion and Power*, Vol. 21, No. 1, 2005, pp. 119-128.

[5]Lotz, W., "Electron-Impact Ionization Cross-Sections and Ionization Rate Coefficients for Atoms and Ions from Hydrogen to Calcium," *Zeitschrift für Physik*, Vol. 216, 1968, pp. 241-247.

[6]Sutton, G. W., and Sherman, A., Engineering Magnetohydrodynamics, Dover Publications, New York, 2006.

[7]Tóth, G., and Odstrõil, D., "Comparison of Some Flux Corrected Transport and Total Variation Diminishing Numerical Schemes for Hydrodynamic and Magnetohydrodynamic Problems," *Journal of Computational Physics*, Vol. 128, 1996, pp. 82-100.

[8]Yee. H. C., "A Class of High-Resolution Explicit and Implicit Shock-Capturing Methods," NASA TM-101088, 1989.

[9]Komurasaki, K., Kobayashi, O., and Fujiwara, T., "Inlet Flow Condition of a Self-Field MPD Thruster," *19th International Symposium on Space Technology and Science*, Yokohama, 1994, ISTS 94-a-45.

[10]Nakayama, T., Toki, K., and Kuriki, K. "Quantitative Imaging of the Magnetoplasmadynamic Flowfield," *Journal of Propulsion and Power*, Vol. 8, No. 6, 1992, pp. 1217-1223.

[11]Kubota, K., Funaki, I., and Okuno, Y., "Hall Effect on the Magnetoplasmadynamic Thruster Flowfields," AIAA paper 2007-4385, 2007.

[12]Funaki, I., "Magnetohydrodynamic Flow in MPD Arcjet," Ph. D. Dissertation, Tokyo Univ., Tokyo, Japan, 1995 (in Japanese).